ACS Catalysis

pubs.acs.org/acscatalysis

Research Article

Sharp Increase in Catalytic Selectivity in Acetylene Semihydrogenation on Pd Achieved by a Machine Learning Simulation-Guided Experiment

Xiao-Tian Li,[§] Lin Chen,[§] Guang-Feng Wei, Cheng Shang, and Zhi-Pan Liu*

Cite This: *ACS Catal.* 2020, 10, 9694−9705

Read Online

ABSTRACT: Pd (metal) is of key value as a heterogeneous hydrogenation catalyst for its high activity and stability. It, however, fails in selective acetylene hydrogenation: at high H_2 pressures and 100% conversion, the dominant product is ethane, not the desirable ethene. Despite decades' efforts, even the structure of the catalyst remains to be veiled by the *in situ* formation of unknown PdH_x and, controversially, PdC_x phases. Here, by combining our recently developed machine learning potential global optimization, microkinetic simulation, and catalysis experiment, we resolve a Pd_4H_3 phase formed under hydrogenation reaction conditions (e.g., 298 K and $p(H_2) > 0.1$ atm), in which the exposed $Pd_4H_3(100)$ open surface is the most responsible for catalyzing the deep hydrogenation to ethane at high H_2 pressures. This finding is rooted in the thermodynamics phase diagram for the Pd−H bulk and surfaces from millions of structure candidates explored by stochastic surface walking (SSW) global optimization and the lowest-energy pathways for the hydrogenation on different surfaces. Guided by the theoretical prediction, Pd catalysts with a large particle size (26 nm) dominated by the close-packed (111) surface are synthesized and tested for selective acetylene hydrogenation in comparison with that of the commercial Pd/C catalyst (particle size ∼2 nm). We show that simple nanostructure engineering improves markedly the selectivity by 16 times, from 4.5% for the commercial Pd catalyst to 76% for our designed Pd catalysts at 100% acetylene conversion and 293 K, showing great promise for machine learning-guided catalyst design. General guidelines to further improve catalyst selectivity are proposed.

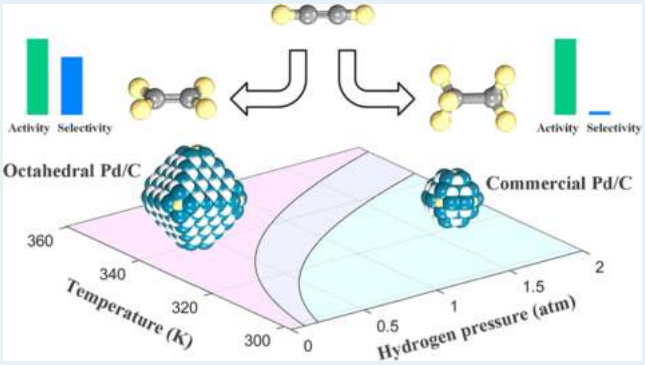

KEYWORDS: *Pd_4H_3, acetylene hydrogenation, NN potential, SSW, LASP*

1. INTRODUCTION

For its industrial importance, the hydrogenation of unsaturated hydrocarbons on palladium catalysts has been extensively studied over 100 years.[1−10] Among them, acetylene (C_2H_2) hydrogenation is of particular interest, which is a text-book example for illustrating the catalytic selectivity: acetylene hydrogenation is desirable to ethene (semihydrogenation) but not to ethane (C_2H_6). A large number of catalysis experiments have shown that pure Pd catalysts exhibit sharply different selectivity in response to H_2 pressures and reaction temperatures, which exhibits the common paradox between the conversion rate and selectivity in catalysis:[11−13] the higher the conversion of acetylene, the poorer the selectivity to ethene it has. Despite decades of study,[11−21] the origin of the selectivity variation of Pd catalysts under different reaction conditions remains elusive. In particular, the Pd-hydride (PdH_x) alloy was long believed to form dynamically under hydrogenation conditions,[12] but little knowledge is now established on the *in situ* surface structures and their relation to catalytic kinetics.

Since Pd is known as a good H storage material, two PdH_x phases are often referred to in experiments at room temperature (e.g., 300 K), α-PdH (H/Pd ∼ 0.03) formed at low H_2 pressures (e.g., 0.01 atm) and β-PdH (H/Pd ∼ 0.6) formed at higher pressures (e.g., 0.1 atm).[22,23] By neutron diffraction, the two phases are found to be both face-centered cubic (fcc) phases with H atoms residing at the octahedral interstitial sites,[24,25] and they can be distinguished by the lattice constant: 3.889 Å for α-$PdH_{0.03}$ and 4.018 Å for β-$PdH_{0.6}$.[22]

As for acetylene hydrogenation on Pd, both α- and β-PdH appear to be active, but the proportion of them depends on the temperature and H_2 pressure. Naturally, the phase would affect the surface structure and thus the catalytic properties markedly. For example, Borodziński et al.[12] observed that on 1% Pd/Al_2O_3 catalyst, the α- to β-PdH transition occurs at 300 K, $p(H_2)$ =

Received: May 15, 2020
Revised: July 28, 2020
Published: August 3, 2020

https://dx.doi.org/10.1021/acscatal.0c02158
ACS Catal. 2020, 10, 9694−9705

0.25 atm, which considerably reduces the acetylene hydrogenation selectivity to ethene from ∼90% to below 50%. Consistently, Freund's group[5,7,26] found that under low-pressure conditions, hydrogenation of pentene to pentane occurs only on Pd nanoparticles supported on an Al_2O_3 film (∼90% (111) and ∼10% (100) facets) but does not occur on a Pd(111) single crystal. They suggested that the high activity (poor selectivity) is due to the weakly bound subsurface H that is available in nanoparticle catalysts, which is evident from temperature-programmed desorption spectral analysis. On the other hand, some recent studies suggest that subsurface C in Pd may cause the selectivity change.[1,6,27] Teschner et al.[27] observed the similar selectivity drop: on 1% Pd/Al_2O_3 at 308 K, p(1-pentyne) = 0.013 atm, the pentyne hydrogenation selectivity to pentene decreases remarkably from ∼100 to ∼10% with an increase of H_2 pressure from 0.01 to 0.13 atm, but by *in situ* X-ray photoelectron spectroscopy analysis, they attributed the decrease in selectivity to the removal of the Pd−C surface phase after the elevation of H_2 pressure. The presence of the Pd−C phase was proposed to hinder the transport and participation of subsurface H in the reactions.[1,28]

In addition to experiments, theoretical calculations based on the density functional theory (DFT) have also been utilized to understand the hydrogenation selectivity since 2000.[28−35] For example, two groups (Sheth et al.[32] and Yang et al.[35]) reported that on the Pd (111) surface (2 × 2 supercell, 25% hydrocarbon coverage, and 25% hydrogen coverage), ethene hydrogenation to ethane has a lower reaction barrier, ∼0.1 eV lower than that for the acetylene hydrogenation to ethene. This data is utilized to explain the poor selectivity of Pd catalysts but is obviously at odds with the relatively good selectivity at low H pressures.[12] Besides, motivated by the experimental findings on the important roles of subsurface C/H species, Yang et al.[35] have also investigated a two-step reaction model for the hydrogenation of acetylene and ethene, namely, the subsurface H atom first diffuses to the clean surface and then reacts with the adsorbates. They reported that the reaction barriers for the hydrogenation of acetylene, vinyl, and ethene by the subsurface H are 0.43, 0.24, and 0.64 eV, respectively, much lower than the barriers associated with the hydrogenation by the surface H (0.73, 0.42, and 0.80 eV), which suggests the high activity of subsurface H. This data, however, fails to explain the poorer selectivity from acetylene to ethene at high H_2 pressure conditions. In fact, these previous studies generally neglected the effect of surface H coverage and did not account for the critical PdH_x bulk phases. It is thus highly desirable to establish the thermodynamics phase diagram for evaluating the equilibrium H distribution in Pd under reaction conditions, both in the bulk and on surfaces.

Here, by using our newly developed global neural network (G-NN) potentials, we are allowed to explore, for the first time, the global potential energy surface (PES) of the Pd−C−H system, from the bulk to surface under catalytic conditions. Focusing on the typical reaction conditions, we rule out the presence of Pd−C bulk phases but identify two stable PdH_x bulk phases from thermodynamics. We reveal all lowest-energy pathways for the hydrogenation of acetylene and ethene under different temperatures and H_2 pressures, linked to two major bulk phases, Pd metal (α phase) and Pd_4H_3 (β phase). The Pd to Pd_4H_3 bulk phase transition causes a dramatic drop in acetylene selectivity to ethene due to the accompanied lattice expansion, which is in favor of the deep hydrogenation to ethane on the open (100) surface. Guided by the theory, the catalytic performances of differently nanosized Pd/C catalysts are tested, and we confirm that the close-packed (111)-dominated large Pd nanoparticles have indeed much better selectivity (76%) to ethene compared with the commercial Pd/C catalyst (4.5%) at 100% conversion.

2. METHODS

2.1. SSW-NN Method. To resolve the bulk and surface structure of Pd−C−H under reaction conditions, the recently developed SSW-NN method as implemented in the Large-scale Atomic Simulation with neural network Potential (LASP) code[36] was utilized for fast global PES exploration, as also demonstrated in our recent work.[37,38] The G-NN potential of the Pd−C−H ternary element was developed by self-learning of the DFT global PES data set, which was generated from the stochastic surface walking (SSW) exploration of the global PESs of different Pd−C−H compositions/structures.[39−41] Self-learning is iteratively performed until the G-NN potential is robust enough to describe the global PES quantitatively. The procedure is briefly introduced below, and more details can be found in Supporting Information (SI) Section 1.

To establish a global PES data set, SSW simulations were performed iteratively on all types of structures (including cluster, layer, and bulk) with a series of different Pd−C−H compositions and varied supercells up to 121 atoms/cell (see SI Table S1). While some systems in the data set, e.g., clusters, are not interested in this work, they are critical for obtaining a transferable Pd−C−H potential. The first-round data set came from DFT-based SSW simulations, while the others were obtained from NN-based SSW simulations in self-learning. In total, more than 10^7 structures were generated by SSW simulations, and 30 138 of them were selected and calculated by high-accuracy DFT calculations as the final global data set for NN potential training.

The G-NN potential was trained based on the global data set using the artificial neural network technique, as described previously.[42−45] To pursue high accuracy of PES, a large set of power-type structure descriptors was adopted for each element, including 100 two-body ones, 86 three-body ones, and 4 four-body ones. A large neural network was utilized, involving two hidden layers (190-50-50-1) with 36 453 network parameters in total. The hyperbolic tangent was utilized as the activation function for the hidden layers, while the linear function was utilized for the output layer. The energy, force, and stress were matched to DFT calculations with the root-mean-square errors (RMSEs) being 2.0 meV, 0.058 eV/Å, and 0.388 GPa, respectively. The systematic benchmark against DFT results was performed and showed the good accuracy of the G-NN potential. For example, we have selected 805 representative PdH_x structures to compute the energy difference between G-NN and DFT calculations, which shows a low RMSE of 2.5 meV/fu, as provided in SI Figure S1. Our detailed comparison between G-NN and DFT calculations for hydrogenation reactions (adsorption energy and reaction barrier) is compiled in SI Table S2.

2.2. Surface Model and Transition-State Search. For surface models, we generally adopted four-layer slabs of (4 × 4) supercells. During simulations, the bottom two layers were fixed at the bulk-truncated position, while the top two layers were fully relaxed (the convergence with respect to the slab thickness was checked and is shown in the SI). Importantly, the surface and subsurface/bulk H atoms varied, as determined from the thermodynamics phase diagram (bulk and surface).

https://dx.doi.org/10.1021/acscatal.0c02158
ACS Catal. 2020, 10, 9694−9705

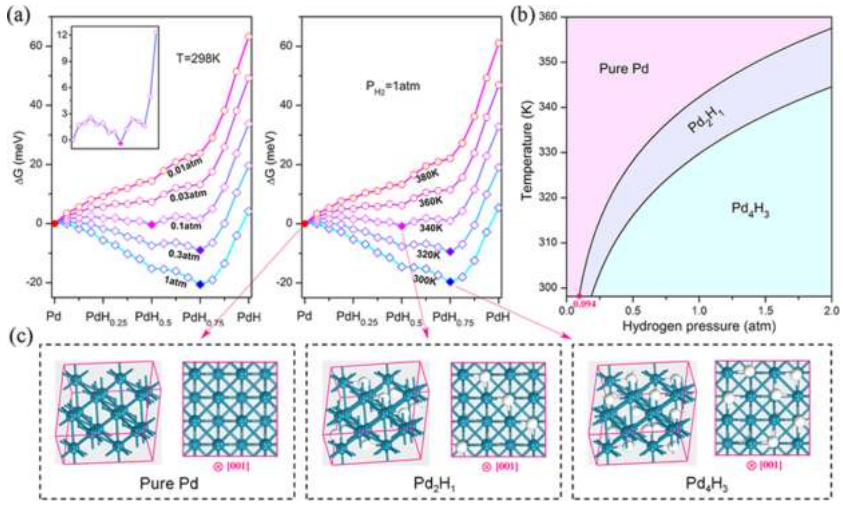

Figure 1. (a) Thermodynamics convex hull diagram for PdH_x phases at different H_2 pressures and temperatures. The inset in the graph is the enlarged view for the curve at 298 K and $p(H_2)$ = 0.1 atm, showing a shallow minimum at Pd_2H. (b) Thermodynamics phase diagram for PdH_x in contact with H_2 at different temperatures and pressures. (c) Atomic structures for pure Pd (lattice a = 3.94 Å), Pd_2H (a = 4.05 Å), and Pd_4H_3 (a = 4.10 Å), all in the fcc lattice. Pd atoms, indigo balls; H atoms, white balls.

The double-ended surface walking (DESW) method[46,47] was utilized to locate the transition states (TS) for hydrogenation reactions. This was achieved by driving two images from the initial state (IS) and final state (FS) toward each other via the addition of bias Gaussian potential consecutively. After the path was connected, the constrained Broyden dimer (CBD) method[48,49] starting from the maximum energy point along the path was then utilized to locate the TS. Thanks to the G-NN potential, these pathway connections and TS locations were facile, and the TSs were further confirmed by vibrational frequency calculations and the optimization-based extrapolation to the correct IS and FS. To address the selectivity and compare with the experiment, we have further converged all of the pathways by DFT. All data reported in this work without explicitly mentioning are from DFT calculations.

2.3. DFT Calculations. DFT calculations were performed with the periodic plane-wave method and the projected augmented wave (PAW)[50] scheme for pseudopotentials, as implemented in the Vienna ab initio simulation package (VASP).[51] The Perdew−Burke−Ernzerhof (PBE) functional at the generalized gradient approximation (GGA)[52] was employed for all calculations, and the plane-wave cutoff was set as 450 eV. The Monkhorst−Pack k-mesh was set to be 30 times the reciprocal lattice vectors (1/30 $Å^{-1}$), while the convergence criterion for the atomic force was 0.01 eV/Å. Zero-point energy (ZPE) was calculated from the phonon spectra using the density functional perturbation theory.

To obtain the free energy profile, we have calculated Gibbs free energies for all the states based on the ZPE-corrected DFT total energy, which was set as the enthalpy at 0 K. The free energy for the gas-phase molecule was computed from thermodynamics by utilizing the standard thermodynamics data at the standard state[53] (e.g., the standard state ΔG values (298 K, 1 bar) for acetylene, ethene, ethane, and hydrogen are −0.52, −0.57, −0.60, and −0.32 eV, respectively). As for the adsorbate on the surface, the free energy was approximated as the enthalpy at 0 K since the thermal effect on enthalpy and the entropy dependence on temperature are small.[54]

3. RESULTS

3.1. PdH_x Phases and Surfaces. To obtain a detailed knowledge of the catalyst under reaction conditions, one needs first to establish the thermodynamics phase diagram of the Pd−C−H ternary system. Thus, our investigations start from the search for the likely PdH_x and PdC_x bulk phases. The presence of PdC_x bulk phases is quickly ruled out since the energetics are much less favorable compared to bulk Pd and graphite (see SI Figure S2 for details). PdH_x bulk phases and their transitions are found to be possible from thermodynamics and are elaborated below.

By SSW-NN, the global PES of PdH_x bulk at different H concentrations has been determined. In our calculations, the H/Pd ratio ranges from 0 to 1.25, in total 41 compositions, and the supercells utilized are up to 72 atoms/cell. For each ratio, more than 10 000 minima were visited to identify the most stable configuration, the so-called global minimum (GM). For all PdH_x systems studied, we found that the GMs are generally in a face-centered close-packing Pd lattice with H occupying the interstitial sites. Here, we must emphasize that due to the flatness of the PES involving H, the ZPE correction is critical and must be taken into account. We found that although the tetrahedral site H is energetically more stable than the octahedral site H without ZPE correction, the most stable configurations turn out to have only octahedral site H after ZPE correction (see SI Figure S3). For example, in a Pd_4 fcc Bravais lattice, the structure with one octahedral site H is 0.086 eV/H more stable than the structure with one tetrahedral site H by ZPE correction. This finding is consistent with the previous works by Caputo et al.[55] and other researchers.[56,57]

With the GM structures obtained from SSW-NN, we then utilized DFT calculations to further validate the structures, and the results after ZPE correction are used to construct the bulk phase diagram under different H_2 pressures and temperatures, as shown in Figure 1a, also known as the thermodynamics convex hull diagram where the chemical potential of H as dictated by H_2 gas is in equilibrium with the H in PdH_x. We show that, not surprisingly, at room temperature (298 K) and low H_2 pressure (0.01 atm), the most thermodynamically favored bulk phase is pure Pd. With an increase of H_2 pressure, H atoms start to

https://dx.doi.org/10.1021/acscatal.0c02158
ACS Catal. 2020, 10, 9694−9705

dissolve into Pd, and at $p(H_2) \approx 0.1$ atm, a phase Pd_2H appears with higher stability than pure Pd. Upon further increasing the H_2 pressure, an important phase Pd_4H_3 forms and becomes the most stable phase for $p(H_2)$ from 0.3 atm to at least 1 atm. On the other hand, keeping the pressure constant at 1 atm, the variation of temperature from 380 to 300 K can also lead to the change of the most stable phase from pure Pd to Pd_2H and to Pd_4H_3, suggesting the high phase mobility of PdH_x upon the change of pressure and temperature.

Overall, the temperature vs pressure phase diagram for PdH_x is summarized and plotted in Figure 1b. As illustrated, with an increase of H_2 pressure and a decrease of temperature, the most stable phase changes from pure Pd to Pd_2H and to Pd_4H_3. At room temperature (298 K), the critical H_2 pressures for pure Pd → Pd_2H and Pd_2H → Pd_4H_3 transitions are 0.094 and 0.186 atm, respectively. Importantly, the window of Pd_2H is rather small, indicating that it is a short-lived transient phase in between Pd and Pd_4H_3.

In Figure 1c, we have highlighted the atomic structure for the three key phases, pure Pd (a = 3.94 Å), Pd_2H (a = 4.05 Å), and Pd_4H_3 (a = 4.10 Å), which are the thermodynamically stable bulk phases in Figure 1b. As can be seen, for Pd_2H, the octahedral site H atoms prefer to align along the [110] direction on the (001) plane, alternating every two rows of atoms. As for Pd_4H_3, the majority of the octahedral sites are occupied by H atoms and the H vacant sites align along ⟨110⟩ directions. By comparing to the experimental characterization, where α phase corresponds to $PdH_{0.03}$ and β phase to $PdH_{0.6}$,[22] our theoretical results suggest that the α phase should be in fact pure Pd but with H covered on the surfaces (see below), while the β phase could be a mixture of Pd_2H and Pd_4H_3 phases according to the experimental conditions. For consistency of the terminology between the theory and experiment, in the following, we also name the H-covered Pd surfaces as the α phase, and the PdH_x with x larger than 0.5 as the β phase.

With the knowledge of bulk PdH_x, we then investigate the surface structures for two key PdH_x phases, i.e., pure Pd (α phase) and Pd_4H_3 (β phase), which are the most stable phases at 298 K, $p(H_2)$ = 0.01 and 1 atm, respectively. By the SSW-NN global search, we have considered a series of possible surface structures with different H coverages on Pd(100), Pd(111), Pd_4H_3(100), and Pd_4H_3(111). Similar to our bulk search, we utilized the SSW-NN simulation to explore more than 10 000 local minima for each surface composition (a typical global PES for H/Pd(111) is shown in SI Figure S4) and the corresponding most stable configurations were then obtained. In these surface global search, the lattice is kept fixed as that of Pd or Pd_4H_3.

Based on the obtained GM structures, the H total adsorption free energies on Pd(100), Pd(111), Pd_4H_3(100), and Pd_4H_3(111) at different H coverages have been computed and are shown in Figure 2a. The most stable atomic configurations are shown in Figure 2b. On Pd(100) and Pd(111) surfaces, the adsorption free energy decreases almost linearly with an increase of surface H up to one monolayer (ML) H coverage, which indicates that there is no obvious H−H interaction between the adsorbed H until the high coverage end of Pd(111). The surface H atoms are adsorbed at the fourfold hollow sites on Pd(100), and at the threefold fcc sites on Pd(111) (see Figure 2b). After 1 ML surface H is present, the subsequent H adsorption becomes thermodynamically unfavorable on Pd(111) but remains almost thermoneutral on Pd(100) until ∼2 ML H coverage (also see the SI for high H coverages above 1.75 ML). This implies that H

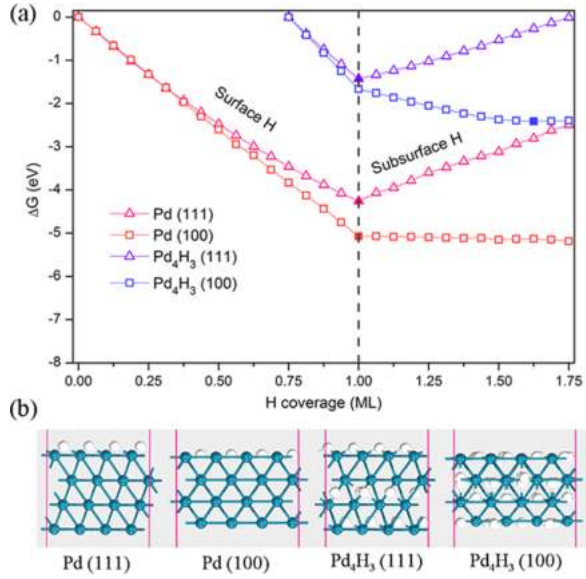

Figure 2. (a) Overall Gibbs free energy changes for H adsorption on Pd(100) and Pd(111) at 298 K, $p(H_2)$ = 0.01 atm and Pd_4H_3(100) and Pd_4H_3(111) at 298 K, $p(H_2)$ = 1 atm with an increase of H coverage on the surface. A solid symbol point is labeled to indicate the most stable H coverages for each surface. (b) Thermodynamically stable surface configurations of Pd(100), Pd(111), Pd_4H_3(100), and Pd_4H_3(111).

can slightly diffuse into the bulk Pd metal from the more open (100) facets.

For Pd_4H_3 surfaces, our investigation starts from the bulk-truncated structure where the surface is terminated by Pd with 0.75 ML subsurface H. After SSW-NN global optimization, these subsurface H atoms redistribute in general, e.g., move to the surface (the kinetics of H migration in Pd is facile from the calculated low reaction barrier, see SI Figure S6). For Pd_4H_3(111), all of the 0.75 ML subsurface H atoms move to surface fcc hollow sites, and 0.25 ML more H can be further added exothermically to reach a full ML. The subsequent H addition into the sublayer then becomes endothermic, and thus, in the final configuration, the bulk H is at least ∼3.3 Å away from the surface (see Figure 2b). Similarly, for Pd_4H_3(100), 1 ML surface H (with 0.75 ML H coming from subsurface), all at the fourfold hollow sites, are also highly favorable. Further adding H, the (100) surface shows the ability to contain subsurface H at the octahedral voids (∼2 Å to the surface, see Figure 2b) until the subsurface is saturated with 0.625 ML H at the second Pd layer, i.e., in total 1.625 ML.

Our theoretical results for PdH_x bulk phases and H/PdH_x surfaces can be compared with the known experimental facts and theoretical studies. For the PdH_x bulk, the transition of the α phase (Pd) to the β phase (Pd_2H and Pd_4H_3) is sensitive to H_2 pressures and temperatures. We predicted the transition conditions from the α phase to the β phase, and two typical conditions related to experimental operation are 298 K, $p(H_2)$ = 0.094 atm and 342 K, $p(H_2)$ = 1 atm. These compare well in general with those reported in experiments, i.e., 301 K, $p(H_2)$ = 0.023 atm[12] and 323 K, $p(H_2)$ = 1 atm,[58] although the experiments appear to favor the transition earlier, which might be due to the kinetic reasons (e.g., the presence of surface defects) and also the intrinsic errors in DFT calculations. As for the surface H adsorption, Wilde et al.[7] using nuclear reaction analysis found that the Pd surface is easily saturated by H even at 94 K and a H_2 pressure of $\sim 10^{-9}$ atm and the bulk H

https://dx.doi.org/10.1021/acscatal.0c02158
ACS Catal. 2020, 10, 9694−9705

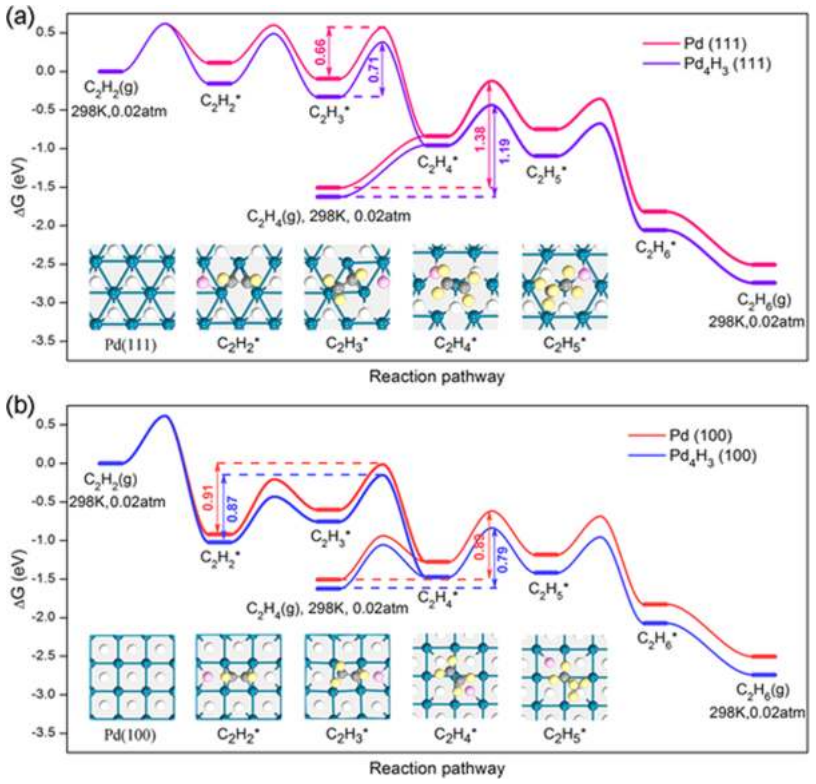

Figure 3. Gibbs free energy profiles for the acetylene hydrogenation on (a) Pd(111), Pd_4H_3(111), (b) Pd(100), and Pd_4H_3(100). The energy zero is referenced to the surface condition (see Figure 2) in equilibrium with the H_2 gas under reaction conditions, i.e., 298 K, $p(H_2)$ = 0.01 atm for pure Pd, and 298 K, $p(H_2)$ = 1 atm for Pd_4H_3, and acetylene/ethene in the gas phase at 298 K, 0.02 atm. The insets show the structural snapshots for reaction intermediates on Pd(111) and Pd(100). H atoms of adsorbates, yellow balls; H atoms bonded with adsorbates, pink balls; other H atoms, white balls; Pd atoms, indigo ball; and C atoms, gray balls.

concentration can keep increasing to ~0.79 (H/Pd) with an increase of H_2 pressure to 2×10^{-8} atm. From our results, at 94 K and 2×10^{-8} atm, the most stable phase is already Pd_4H_3 (0.75) and the surface is always 1 ML saturated by H. The previous DFT study on TiO_2-supported Pd_4 cluster[59] also found that Pd_4 can adsorb 2−3 H atoms at 300 K, $p(H_2)$ = 0.017 atm, which is consistent with the Pd/H ratio in our Pd_2H and Pd_4H_3 bulk phases. The consistency between the theory and experiment suggests that the β phase could form at low temperatures and low H_2 pressures, confirming the predictive ability of thermodynamics.

3.2. Hydrogenation Reactions. We now focus on the hydrogenation of acetylene/ethene on four representative surfaces, i.e., Pd(100), Pd(111), Pd_4H_3(100), and Pd_4H_3(111), to understand the hydrogenation activity and selectivity of α and β-PdH_x phases. With the help of G-NN potentials, we have utilized the SSW-NN-based reaction sampling method[38] to explore all the likely pathways at the high turnover conditions as concerned in the experiment. This corresponds to the condition where H_2 pressure is much higher than that of acetylene/ethene and thus the surface has a high H coverage but low acetylene/ethene coverage. All reaction barriers were determined by locating the TS, and DFT calculations were utilized to confirm all computed energetics.

In general, we found that the hydrogenation reaction follows the Horiuti−Polanyi mechanism,[60] namely, via sequential hydrogenation from acetylene to vinyl (C_2H_3), ethene, ethyl (C_2H_5), and ethane. Importantly, with the surface H coverage being explicitly considered here, i.e., treated as equilibrium with the gas-phase H_2 under reaction conditions, we can now reveal how the reaction kinetics are affected quantitatively by the surface facets and the reaction conditions (temperature and pressure). Figure 3 shows the Gibbs free energy profile for the lowest pathways of the acetylene and ethene hydrogenation on the four surfaces under the reaction conditions, i.e., 298 K, $p(H_2)$ = 0.01 atm for pure Pd and 298 K, $p(H_2)$ = 1 atm for Pd_4H_3. In Table 1, we have listed the key kinetic parameters, i.e., the adsorption energy, adsorption free energy, and overall barrier, on the four surfaces.

Taking acetylene hydrogenation on Pd(111) as an example, we elaborate on the reaction mechanism and free energetics in

Table 1. Adsorption Energy (E_{ad}), Free Adsorption Energy (G_{ad}), and Overall Barrier (G_a) for Acetylene/Ethene Hydrogenation on (100) and (111) Surfaces of Pd (α Phase) and Pd_4H_3 (β Phase)[a]

	acetylene			ethene		
surface	E_{ad}	G_{ad}	G_a	E_{ad}	G_{ad}	G_a
Pd(111)	−0.51	0.11	0.66	0.00	0.88	1.38
Pd(100)	−1.54	−0.92	0.91	−0.44	0.23	0.89
Pd_4H_3(111)	−0.78	−0.16	0.71	0.00	0.67	1.19
Pd_4H_3(100)	−1.64	−1.02	0.87	−0.52	0.15	0.79

[a]The energy unit is electronvolts. The free energy is with respect to the gas-phase acetylene, ethene, and H_2 at typical reaction conditions (T = 298 K; $p(H_2)$ = 0.01 atm for Pd and 1 atm for Pd_4H_3; p(acetylene) and p(ethene) are set as 0.02 atm). The acetylene/ethene adsorption configuration on Pd(111) and Pd(100) is also provided in SI Figure S8.

https://dx.doi.org/10.1021/acscatal.0c02158
ACS Catal. 2020, 10, 9694−9705

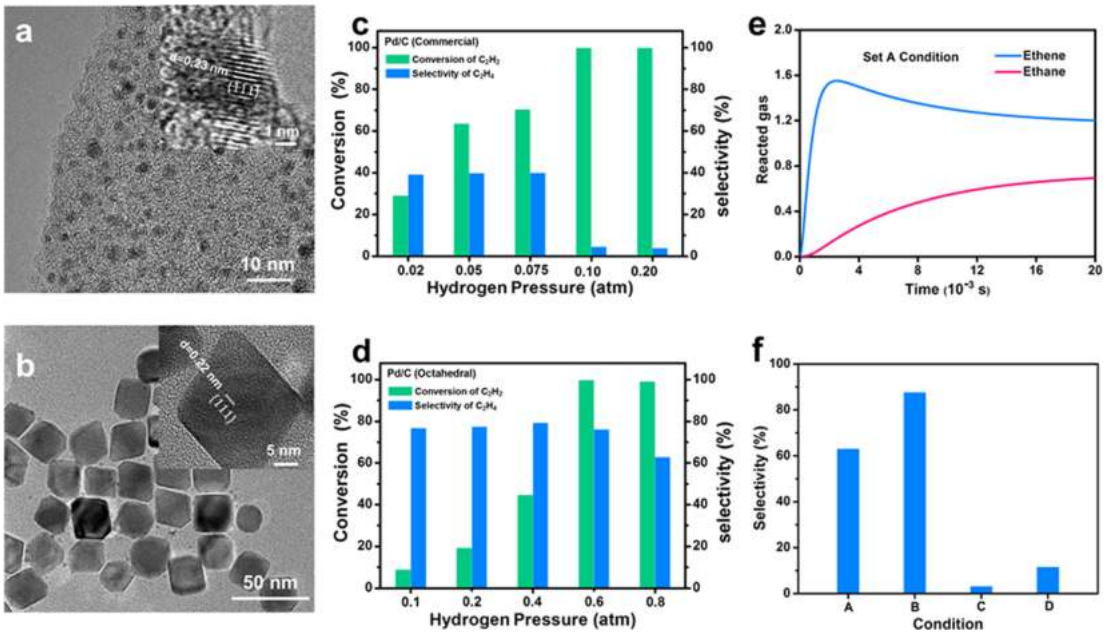

Figure 4. Experiments and microkinetic simulations for acetylene hydrogenation on Pd catalysts. The TEM images for (a) commercial Pd supported on carbon and (b) octahedral Pd (the insets are the enlarged views from high-resolution (HR)-TEM images); the conversion of acetylene and the selectivity to ethene on (c) commercial Pd/C and (d) octahedral Pd/C at 293 K, $p(C_2H_2) = 0.02$ atm, varied $p(H_2)$, and a gas hourly space velocity (GHSV) of 120 000 h^{-1}; and the microkinetic simulation results for (e) time-resolved reaction curve at the set **A** condition (Pd phase with (111)/(100) = 9:1 and $C_2H_2/H_2 = 2:5$) and (f) acetylene selectivity to ethene from the set **A**, **B**, **C**, and **D** conditions (see the text for details).

detail. In the lowest-energy pathway, the reaction starts at a surface hydrogen vacancy (H_v) site, which requires a free energy cost of 0.25 eV to form. Acetylene can then adsorb at the available fcc hollow site with a gain in the free energy of 0.14 eV. The nearby surface H atoms can react with the adsorbed acetylene to form vinyl and ethene successively. The reaction is facile and progressively exothermic. The rate-determining step occurs from vinyl to ethene with a barrier of 0.66 eV. Meanwhile, the consumed surface H can be refilled by the dissociation of H_2 due to the low H_2 dissociation barrier (0.32 eV). Next, for ethene hydrogenation, as the surface is fully covered by H, ethene adsorption is strongly endothermic by 0.88 eV in free energy. The adsorbed ethene can react with the nearby H with a barrier of 0.5 eV to ethyl, which can then overcome a barrier of 0.39 eV to ethane. The overall barrier is 1.38 eV from ethene to ethane, which is considerably higher than the barrier from acetylene to ethene (0.66 eV). The overall barrier remains similar even for the ethene hydrogenation occurring at a H_v site (see SI Figure S9). These results indicate that at 298 K, $p(H_2) =$ 0.01 atm, Pd(111) with precovered H can have a high selectivity to convert acetylene to ethene but not to ethane (we will further demonstrate this using the microkinetic simulations below).

We note that the hydrogenation of acetylene and ethene on Pd(111) has been also studied previously by DFT calculations.[29,31−35] However, the previous studies generally did not consider explicitly the coverage effect (i.e., with low H and acetylene/ethene coverage as limited by the modeled supercell). For example, sheth et al.[32] found that the acetylene and ethene adsorption energies on clean Pd(111) (2 × 2 supercell) are −1.79 and −0.85 eV, respectively, whereas they turn out to be −0.51 and +0.21 eV on the 1 ML H-covered (111) surface. Consistently, their results for the hydrogenation barriers from acetylene to ethene and from ethene to ethane are 0.88 and 0.76 eV, respectively, also very different from our results. On the other hand, our calculated hydrogenation energetics on clean Pd(111) are indeed consistent with the previous results,[32] as shown in SI Table S3. This suggests that the realistic H coverage at the reaction conditions is critical to understand the hydrogenation kinetics.

Next, we discuss the results on the other three surfaces, which are also shown in Figure 3. Although the same sequential hydrogenation mechanism is followed on these surfaces, the energetics can vary quite significantly. We summarize the key findings as follows.

(i) On Pd(100) at 1 ML H coverage, acetylene can adsorb strongly with an overall free energy gain of 0.92 eV by removing a preadsorbed H, where acetylene adsorbs across two bridge sites, linking with four Pd atoms (see Figure 3b inset C_2H_2*). The overall barrier is 0.91 eV from adsorbed acetylene to ethene, much higher than that (0.66 eV) on Pd(111). Similarly, ethene adsorption is also improved on Pd(100) with a free energy loss of only 0.23 eV, where ethene adsorbs at the top site of a surface Pd atom (see Figure 3b inset C_2H_4*), and the overall barrier from ethene to ethyl is 0.89 eV, much lower than that (1.38 eV) on Pd(111).

(ii) On Pd_4H_3(111), the energetics are similar to those on Pd(111), except that the acetylene hydrogenation overall barrier is higher by 0.05 eV, while the ethene hydrogenation overall barrier is lower by 0.19 eV.

(iii) On Pd_4H_3(100), the energetics are similar to those on Pd(100), except that both the hydrogenation barriers of acetylene and ethene are slightly lower, by 0.04 and 0.10 eV, respectively.

For clarity, we summarize the overall barrier of the hydrogenation reactions on the four surfaces in Table 1. It shows clearly that acetylene is easiest to hydrogenate on Pd(111) to ethene. The overall barrier for acetylene to ethene increases in the order Pd(111) < Pd_4H_3(111) < Pd_4H_3(100) <

https://dx.doi.org/10.1021/acscatal.0c02158
ACS Catal. 2020, 10, 9694−9705

Pd(100). In contrast, ethene is the easiest to hydrogenate to ethane on Pd_4H_3(100) and the overall barrier for ethene to ethane increases in the order Pd_4H_3(100) < Pd(100) < Pd_4H_3(111) < Pd(111). Interestingly, the two orders are just opposite, implying that the hydrogenation selectivity should be sensitive to both the surface termination and the PdH_x phases (thus reaction conditions). The high pressures and the (100) exposure could lead to poor selectivity.

As a proof to concept, we considered conducting experiments to measure the hydrogenation selectivity of Pd catalysts at different H_2 pressures. To avoid the (100) surface and reduce the probability of phase transition from Pd to Pd_4H_3, the guidelines from the theory are to increase the Pd particle size and maximize the (111) exposure.

3.3. Catalytic Hydrogenation Experiments on Pd Catalysts. We managed to examine the catalytic hydrogenation for two different Pd catalysts (the details of the catalyst preparation procedure are provided in SI Section 7), namely, the commercial Pd and the octahedral Pd samples. The commercial Pd supported on Vulcan XC-72R carbon has very small Pd particles (~1.8 nm as estimated from transmission electron microscopy (TEM) images), as shown in the TEM image (Figure 4a). This is consistent with the X-ray diffraction (XRD) results, where no discernible diffraction peak is detected (SI Figure S11). These very small Pd particles appear to be round in shape with different lattice fringes. By contrast, the octahedral Pd was synthesized in our lab, which was also supported on Vulcan XC-72R carbon, and the Pd particles were designed to be large in size and octahedral in shape. This can be seen in the TEM image in Figure 4b, where the octahedral Pd preferentially exposes (111) facets and has a size of ~21.6 nm as estimated both by TEM images (SI Figure S12) and the Scherrer equation using the XRD data. In both samples, TEM shows the (111) plane distance of 0.22−0.23 nm, consistent with the theoretical value (0.23 nm). Besides, it is also noticed that in our octahedral Pd sample, the carbon support covers the Pd nanoparticle surface (as seen from TEM, SI Figure S13), indicating their close contact in geometry. Obviously, the two samples are quite different in both particle sizes and the exposed facets.

We then carried out a series of acetylene hydrogenation reactions on the two Pd catalyst samples, and the results are shown in Figure 4c,d. All experiments were carried out at 293 K, with a feed gas composition of 2% C_2H_2 (in volume) and varying amounts of H_2 and N_2 (for balance) at a space velocity of 1 200 000 mL/g/h. The typical time-dependent behavior of the catalysts can be seen in SI Figure S16.

For the commercial Pd/C, as seen in Figure 4c, with an increase of H_2 pressure from 0.02 to 0.075 atm, the selectivity from acetylene to ethene is almost constant at ~40%, while the acetylene conversion largely increases from 29.1 to 70.5%. As the H_2 pressure increases to 0.1 atm, however, the selectivity decreases suddenly to 4.5% with the conversion reaching 100%. Thereafter, the higher H_2 pressure up to 0.2 atm does not lead to obvious variations in both the conversion and selectivity. The 0.1 atm condition for the sudden drop of acetylene selectivity coincides with our theoretical data where the phase transition from the α phase to the β phase occurs, implying that the pure Pd phase has a higher selectivity to ethene than the β phase (Pd_4H_3). These results are consistent with the previous experiment by Zhang et al.,[61] showing the poor selectivity of small Pd nanoparticles in Pd/Al_2O_3.

For the octahedral Pd/C, as seen in Figure 4d, with the lift of H_2 pressure from 0.1 to 0.6 atm, the selectivity from acetylene to ethene is quite stable, above 76%, while the acetylene conversion increases from 9 to 100%. Only when H_2 pressure is up to 0.8 atm, a mild drop in selectivity to 62.8% is observed. The turnover frequency (TOF) for acetylene hydrogenation was measured to be 38 s^{-1} (see SI Table S5 for experimental details), which is in line with our theoretical data on Pd(111), i.e., 0.66 eV barrier and thus ~27 s^{-1} TOF deduced from microkinetics. By comparing with commercial Pd/C, the octahedral Pd/C exhibits much better selectivity for acetylene hydrogenation to ethene at the high H_2 pressures (>0.1 atm), reaching a selectivity of 76.2% at 100% acetylene conversion.

The large selectivity difference between the two catalysts suggests the strong structure sensitivity of semihydrogenation on Pd nanoparticles (the structure sensitivity was also found on Pt nanoparticles[62,63]). Since the octahedral Pd/C catalyst has a relatively large particle size and the preferential (111) exposure, one would expect that the crystal surfaces, i.e., (111) or (100), and the bulk phases, i.e., Pd or PdH_x, may affect the selectivity significantly. From our theoretical results (see Table 1), the two (111) surfaces, Pd(111) and Pd_4H_3(111), have higher selectivity to ethene than the two (100) surfaces. To understand these experimental results quantitatively, we then performed microkinetic simulations based on the theoretical data. The results are discussed below.

Our microkinetic simulations utilized a continuous stirred tank model, in which the feed gas (2×10^6 molecules in total) inflows the tank and the reacted gas outflows in every time interval. The kinetic parameters are summarized in SI Table S4. According to our experimental conditions, the simulation has the following setups: the feed gas consists of C_2H_2 and H_2 in the ratios from 2:5 to 2:20 (corresponding to $p(H_2)$ at 0.05 and 0.2 atm); the contact time is taken to be 0.01 s, i.e., in every 10^{-6} s, we added 0.01% feed gas into the system and removed 0.01% reacted gas; and the (111)/(100) ratios are set to be 9:1 and 19:1. The lower (111)/(100) ratio is estimated from thermodynamics according to the Wulff construction rule,[64] and the higher ratio corresponds to the typical particle measured from TEM images of the octahedral Pd/C sample. We thus have four different sets of simulation conditions, namely,

A: Pd phase with (111)/(100) = 9:1 and C_2H_2/H_2 = 2:5;

B: Pd phase with (111)/(100) = 19:1 and C_2H_2/H_2 = 2:5;

C: Pd_4H_3 phase with (111)/(100) = 9:1 and C_2H_2/H_2 = 2:20; and

D: Pd_4H_3 phase with (111)/(100) = 19:1 and C_2H_2/H_2 = 2:20.

Our microkinetic results are shown in Figure 4e,f. Figure 4e illustrates a typical time-resolved reaction curve as represented by the set **A** condition. As shown, the content of ethene increases first to 1.55×10^6 molecules before 2.5×10^{-3} s and then decreases smoothly to 1.20×10^6 molecules at 2×10^{-2} s. At the same time, the content of ethane gradually increases from 0 to 0.69×10^6 molecules at 2×10^{-2} s. At equilibrium, the surface H coverage reaches to 0.998 and 0.999 ML on Pd(111) and Pd(100), respectively, which is consistent with our thermodynamic diagram in Figure 2. Figure 4f shows the acetylene selectivity values to ethene at the **A**, **B**, **C**, and **D** sets of conditions, which turn out to be 63.4, 87.9, 3.4, and 11.8%, respectively. It shows clearly that (i) the Pd_4H_3 phase has much poorer selectivity (below 11.8%) compared to the Pd phase (above 63.4%) and that (ii) the higher (111)/(100) ratio can always improve the selectivity to ethene.

Now, we are in the position to discuss our experimental observations in the context of microkinetic results. For the

https://dx.doi.org/10.1021/acscatal.0c02158
ACS Catal. 2020, 10, 9694−9705

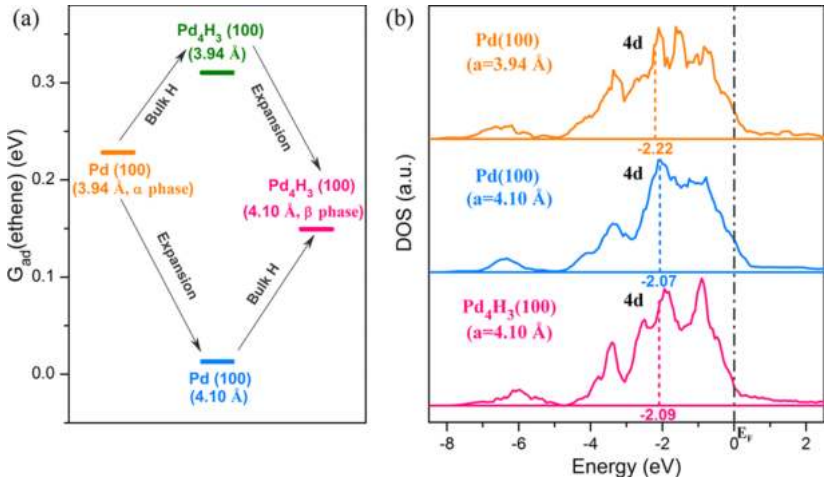

Figure 5. (a) Ethene adsorption free energy G_{ad}(ethene) on four different surfaces at 298 K, p(C_2H_4) = 0.02 atm, showing the effect of the varying lattice: Pd (100) (a = 3.94 Å, α phase), Pd (100) with expanded lattice (a = 4.10 Å), Pd_4H_3 (100) with shrunk lattice (a = 3.94 Å), and Pd_4H_3 (100) (a = 4.10 Å, β phase). (b) Projected density of states (DOS) of Pd 4d states on three surfaces: Pd (100) (a = 3.94 Å), Pd (100) with expanded lattice (a = 4.10 Å), and Pd_4H_3 (100) (a = 4.10 Å). The position of the d-band center is denoted by the dashed line.

commercial Pd/C catalyst, a sudden drop in selectivity at p(H_2) = 0.1 atm is well reproduced by microkinetic simulations, confirming that the phase transition from Pd to Pd_4H_3 can explain the large selectivity reduction from 40 to 4.5%. The higher selectivity in microkinetic simulations (>60%) than that in experiments (40%) may be caused by the low (111)/(100) ratio in small Pd nanoparticles. In fact, the morphology of small nanoparticles and thus the (111)/(100) ratio are known to vary under reaction conditions due to the adsorption of reactants. Our previous work on Pt_{44} particles (~1 nm) has found that under H_2 conditions the particles prefer to expose the (100) surface but revert to (111)-dominant particles without H_2.[6565]

For the octahedral Pd/C catalyst, the experimental results (76.2% selectivity) indeed do not support the formation of the Pd_4H_3 phase but are in line with the Pd phase at the condition sets **A** and **B**, where the selectivity from microkinetics simulations is above 63%. The lack of Pd_4H_3 formation is interesting, implying that the large Pd particles with (111) dominance inhibit the migration of H deep into the bulk. The selectivity decreases slowly only when p(H_2) is high, above 0.6 atm. From our results, if the lattice is fixed, the H diffusion into the Pd(111) surface is highly endothermic and is also not favorable into Pd(100) (see Figure 2a and SI Figure S5), which suggests that the H diffusion into the Pd bulk is kinetically hindered as long as the lattice expansion is frustrated. This is reasonable considering that the Pd lattice is 3.9% smaller compared to Pd_4H_3 and the H cannot be stable in the Pd bulk without lattice expansion. In agreement with our results, Freund's group[5] has reported that the subsurface H is not present in the Pd(111) single crystal. We thus expect that both the large size (21.6 nm) and the Vulcan XC-72R carbon support (TEM in SI Figure S13) for the octahedral Pd sample may help to maintain the Pd bulk lattice and thus prevent kinetically the formation of Pd_4H_3 below 0.6 atm H_2 pressure. The difficulty to form the PdH phase for octahedral Pd/C is indeed confirmed by our electrochemistry experiment by measuring the underpotential deposited H (UPD) peaks (see SI Figure S15).

4. GENERAL DISCUSSIONS

4.1. Origin of the Poor Selectivity of the Pd_4H_3 Phase.

As for the origin of the poor selectivity of Pd catalysts, a common thought from experimental literature works is related to the too-high activity of subsurface H that can deep hydrogenate ethene to ethane. For example, Freund et al.[5,7,26] observed that nanoparticle Pd catalysts with subsurface H have a high activity for alkene hydrogenation to ethane. However, there is no evidence from experiments that the subsurface H participates directly in the hydrogenation reaction. In fact, from our theory and experiment, the formation of the PdH_x phase is a sign for the presence of subsurface H. The hydrogenation reactions on Pd and Pd_4H_3 surfaces, no matter (111) and (100), occur at the same H surface coverage (1 ML), but the selectivity differs significantly, as seen from Figure 4f. We conclude that the poor selectivity solely comes from the presence of the new PdH phase, the open (100) surface of which offers a particularly low barrier channel for the ethene hydrogenation to ethane. It is worth mentioning that disordered phases, possibly formed under reaction conditions, may also play roles in catalytic conversion.[66,67] Since our experiment and theoretical simulations are highly consistent at the 298 K reaction temperature, we believe that the major contribution to the overall activity and selectivity is from the ordered crystal faces on Pd and Pd_4H_3 phases.

In fact, the data in Table 1 has revealed the characteristics of Pd_4H_3 phase catalysis. It helps to increase the barrier of acetylene to ethene on (111) by 0.05 eV (0.66−0.71 eV) but reduces that for ethene to ethane on (100) by 0.1 eV (0.89−0.79 eV). As we found in microkinetic simulations, this change turns over the selectivity on Pd_4H_3 since the ethene obtained from acetylene can desorb from (111) and then deep hydrogenates to ethane with a lower barrier on (100) in the secondary process.

We can now analyze the ethene hydrogenation on Pd(100) and Pd_4H_3(100), both surfaces being precovered by 1 ML H atoms. The most obvious differences between the two surfaces are the lattice constant and the bulk H concentration; we thus compared the ethene hydrogenation on four different (100) surfaces (with the lattice being manually varied), i.e., Pd (100) (a = 3.94 Å), Pd (100) with expanded lattice (a = 4.10 Å), Pd_4H_3 (100) with shrunk lattice (a = 3.94 Å), and Pd_4H_3(100) (a = 4.10 Å). As shown in SI Figure S10, we found that the reaction barriers for the four surfaces are 0.89, 0.64, 0.96, and 0.79 eV, respectively. Interestingly, the major difference among these

https://dx.doi.org/10.1021/acscatal.0c02158
ACS Catal. 2020, 10, 9694−9705

surfaces lies in the ethene adsorption energy but not in the elementary reaction barrier from adsorbed ethene to ethane (being rather constantly ~0.65 eV). The expanded lattice leads to exothermic adsorption of ethene in free energy, as plotted in Figure 5a, which effectively lowers the overall barrier from the gas-phase ethene to ethane. We notice that the relation between the metal lattice and adsorbate adsorption energy has been well documented[68] and known as a consequence of the relative shift of the metal d-band center. Indeed, by plotting the d-band of the surface Pd atom (see Figure 5b), we found that the Pd d-band center does shift up toward the Fermi level from −2.22 to −2.07 eV when the Pd(100) lattice expands from 3.94 to 4.10 Å. In contrast, the presence of subsurface/bulk H in Pd_4H_3(100) only slightly shifts the d-band center downward from −2.07 to −2.09 eV, implying that the direct repulsion from the subsurface/bulk H could be more important in destabilizing the ethene adsorption by 0.14 eV.

4.2. Relevance of the Pd_4H_3 Phase in Industrial Conditions. In industries, there are typically two basic types of hydrogenation conditions, depending on the position of the hydrogenation reactor in the ethene production plant: the front-end condition operating at high H_2 pressures (0.10−0.35 atm) and the tail-end condition at low H_2 pressures (0.01−0.04 atm).[12,69] The front-end condition, as shown in this work, favors the formation of the Pd_4H_3 phase for small Pd nanoparticles and thus suffers from the selectivity problem. On the other hand, the tail-end condition, due to a lack of hydrogenation ability, has the risk to form polymers between acetylene and thus poisons the catalyst. From our calculations, we have found that on Pd(100), two acetylene molecules can recombine to form C_4H_4 with a modest barrier of 1.08 eV. It is thus reasonable that a high H_2 pressure to maintain the precovered surface H is a key approach to prevent the polymerization process.

A key finding from this work is that the minority sites, i.e., (100) surface, play the key role in determining the hydrogenation selectivity. This is because, unlike acetylene, ethene prefers to adsorb at a top site (i.e., single Pd is enough), with the π-bonded configuration under the high-H_2-pressure conditions and thus maintains hydrogenation activity as long as the exposed Pd atoms on (100) are available. As a support to our results, the previous experiments by Freund's group[70] and other groups[12] have demonstrated that the ethene hydrogenation activity of Pd is independent of the particle size. Indeed, only via crystal engineering to maximize the (111) surface area, our own experiment demonstrates that the hydrogenation selectivity can be significantly improved.

We are still left with the most challenging question, how to further increase the hydrogenation selectivity, e.g., to 100%. Undoubtedly, this is difficult since (100) as the second-lowest surface energy facet in the Pd metal cannot be avoided totally in nanoparticle catalysts and, in fact, as the particle becomes smaller, the (100) and other minority sites should even increase in population.[65] We note that the industrial PdAg catalysts achieve a higher selectivity (~80%) via Ag alloying where Ag was believed to block the active sites for ethene hydrogenation. From this work, it is very likely that the Ag element may have a dual role in catalysis: (i) blocks (100) sites but leaves (111) sites available and (ii) reduces the ethene adsorption and prevents the Pd_4H_3 bulk phase formation. The mechanism of the Ag promotion effect is now investigated in our lab.

5. CONCLUSIONS

To recap, this work resolves the selectivity origin of Pd-catalyzed acetylene semihydrogenation using a bottom-up approach, from the PES global exploration in theory to the catalysis experiment confirmation. To overcome the current theoretical limitations in determining the *in situ* catalyst structure, we establish the first Pd−C−H ternary G-NN potential, based on which the SSW-NN simulation helps to reveal the bulk and surface phase diagrams under relevant experimental conditions. After determining the atomic structures of PdH surfaces, we are able to identify the lowest-energy pathways for acetylene hydrogenation to ethene and ethane on different surfaces. This leads to the prediction for the highest selectivity on Pd(111) but the poorest selectivity on Pd_4H_3(100). Both the catalysis experiment and microkinetic simulation then confirm that the selectivity can be significantly improved via nanostructure engineering, namely, increasing the particle size and reducing the open (100) surface exposure. With the latest advancement in machine learning simulations, we demonstrate that the long-standing puzzles in heterogeneous catalysis associated with those occurring dynamically in the reaction can now be resolved, which holds great promise to design rationally better catalysts. The key findings of the work are outlined below in detail.

(i) We characterize the conventionally termed α-phase and β-phase in Pd hydrogenation as the Pd metal and Pd_4H_3, respectively. The surfaces of both phases are fully covered by H atoms (1 ML) under typical hydrogenation conditions (298 K and $p(H_2) > 0.01$ atm).

(ii) On the 1 ML H-covered Pd(111) and Pd(100) at 298 K, $p(H_2) = 0.01$ atm and Pd_4H_3(111) and Pd_4H_3(100) at 298 K, $p(H_2) = 1$ atm, the free energy overall barriers for acetylene to ethene are 0.66, 0.91, 0.71, and 0.87 eV, while those for ethene to ethane are 1.38, 0.89, 1.19, and 0.79 eV for the reaction at $p(C_2H_2) = p(C_2H_4) = 0.02$ atm. Microkinetic simulations confirm further the preference for the Pd metal and (111) surface to achieve high selectivity for acetylene hydrogenation.

(iii) Experimentally, two Pd/C samples are compared for catalytic performance. The large Pd octahedral nanoparticles (~22 nm), as guided by the theory in design, do exhibit as high as 76.5% selectivity at 100% acetylene conversion at room temperature, while the small Pd nanoparticles (<2 nm) have a very low selectivity of 4.5%.

(iv) The origin of the poor selectivity for the typical Pd catalyst is attributed to the facileness of the phase transition from Pd to Pd_4H_3 in very small nanoparticles, where ethene has a better adsorption ability on the open Pd_4H_3(100) surface caused by the 4% expanded lattice of the Pd_4H_3 phase. We propose that the general design principle for a highly selective Pd-based catalyst is either to avoid the (100) surface by site blocking or to reduce further the ethene adsorption on (100) via electronic structure tuning, e.g., Ag alloying to inhibit the Pd_4H_3 phase.

■ ASSOCIATED CONTENT

Supporting Information

The Supporting Information is available free of charge at https://pubs.acs.org/doi/10.1021/acscatal.0c02158.

Theoretical methodology and the construction of the ternary Pd−C−H G-NN potential, formation of Pd−C bulk phases, ZPE correction for the PdH_x system, stability

https://dx.doi.org/10.1021/acscatal.0c02158
ACS Catal. 2020, 10, 9694−9705

and migration of H in/on the Pd bulk/surface, hydrogenation reactions under different conditions, kinetic parameters used in microkinetic simulations; experimental details, including the synthetic procedure and characterization, and *XYZ* coordinates for all of the structures in Figure 3 (PDF)

AUTHOR INFORMATION

Corresponding Author

Zhi-Pan Liu − *Collaborative Innovation Center of Chemistry for Energy Material, Shanghai Key Laboratory of Molecular Catalysis and Innovative Materials, Key Laboratory of Computational Physical Science, Department of Chemistry, Fudan University, Shanghai 200433, China;* orcid.org/0000-0002-2906-5217; Email: zpliu@fudan.edu.cn

Authors

Xiao-Tian Li − *Collaborative Innovation Center of Chemistry for Energy Material, Shanghai Key Laboratory of Molecular Catalysis and Innovative Materials, Key Laboratory of Computational Physical Science, Department of Chemistry, Fudan University, Shanghai 200433, China*

Lin Chen − *Collaborative Innovation Center of Chemistry for Energy Material, Shanghai Key Laboratory of Molecular Catalysis and Innovative Materials, Key Laboratory of Computational Physical Science, Department of Chemistry, Fudan University, Shanghai 200433, China*

Guang-Feng Wei − *Shanghai Key Laboratory of Chemical Assessment and Sustainability, State Key Laboratory of Pollution Control and Resources Reuse, School of Chemical Science and Engineering, Tongji University, Shanghai 200092, China*

Cheng Shang − *Collaborative Innovation Center of Chemistry for Energy Material, Shanghai Key Laboratory of Molecular Catalysis and Innovative Materials, Key Laboratory of Computational Physical Science, Department of Chemistry, Fudan University, Shanghai 200433, China;* orcid.org/0000-0001-7486-1514

Complete contact information is available at: https://pubs.acs.org/10.1021/acscatal.0c02158

Author Contributions

[§]X.-T.L. and L.C. are co-first authors with equal contribution to this work.

Notes

The authors declare no competing financial interest.

ACKNOWLEDGMENTS

This work was supported by the National Key Research and Development Program of China (2018YFA0208600) and the National Science Foundation of China (21533001 and 91745201).

REFERENCES

(1) Teschner, D.; Borsodi, J.; Wootsch, A.; Révay, Z.; Hävecker, M.; Knop-Gericke, A.; Jackson, S. D.; Schlögl, R. The Roles of Subsurface Carbon and Hydrogen in Palladium-Catalyzed Alkyne Hydrogenation. *Science* **2008**, *320*, 86.

(2) Studt, F.; Abild-Pedersen, F.; Bligaard, T.; Sørensen, R. Z.; Christensen, C. H.; Nørskov, J. K. Identification of Non-Precious Metal Alloy Catalysts for Selective Hydrogenation of Acetylene. *Science* **2008**, *320*, 1320.

(3) Chen, Q.-A.; Ye, Z.-S.; Duan, Y.; Zhou, Y.-G. Homogeneous Palladium-Catalyzed Asymmetric Hydrogenation. *Chem. Soc. Rev.* **2013**, *42*, 497−511.

(4) Zhang, L.; Zhou, M.; Wang, A.; Zhang, T. Selective Hydrogenation over Supported Metal Catalysts: From Nanoparticles to Single Atoms. *Chem. Rev.* **2020**, *120*, 683−733.

(5) Doyle, A. M.; Shaikhutdinov, S. K.; Jackson, S. D.; Freund, H.-J. Hydrogenation on Metal Surfaces: Why are Nanoparticles More Active than Single crystals? *Angew. Chem., Int. Ed.* **2003**, *42*, 5240−5243.

(6) Teschner, D.; Révay, Z.; Borsodi, J.; Hävecker, M.; Knop-Gericke, A.; Schlögl, R.; Milroy, D.; Jackson, S. D.; Torres, D.; Sautet, P. Understanding Palladium Hydrogenation Catalysts: When the Nature of the Reactive Molecule Controls the Nature of the Catalyst Active Phase. *Angew. Chem., Int. Ed.* **2008**, *47*, 9274−9278.

(7) Wilde, M.; Fukutani, K.; Ludwig, W.; Brandt, B.; Fischer, J.-H.; Schauermann, S.; Freund, H.-J. Influence of Carbon Deposition on the Hydrogen Distribution in Pd Nanoparticles and Their Reactivity in Olefin Hydrogenation. *Angew. Chem., Int. Ed.* **2008**, *47*, 9289−9293.

(8) Studt, F.; Abild-Pedersen, F.; Bligaard, T.; Sørensen, R. Z.; Christensen, C. H.; Nørskov, J. K. On the Role of Surface Modifications of Palladium Catalysts in the Selective Hydrogenation of Acetylene. *Angew. Chem., Int. Ed.* **2008**, *47*, 9299−9302.

(9) Crespo-Quesada, M.; Yarulin, A.; Jin, M.; Xia, Y.; Kiwi-Minsker, L. Structure Sensitivity of Alkynol Hydrogenation on Shape- and Size-Controlled Palladium Nanocrystals: Which Sites Are Most Active and Selective? *J. Am. Chem. Soc.* **2011**, *133*, 12787−12794.

(10) Feng, Q.; Zhao, S.; Wang, Y.; Dong, J.; Chen, W.; He, D.; Wang, D.; Yang, J.; Zhu, Y.; Zhu, H.; Gu, L.; Li, Z.; Liu, Y.; Yu, R.; Li, J.; Li, Y. Isolated Single-Atom Pd Sites in Intermetallic Nanostructures: High Catalytic Selectivity for Semihydrogenation of Alkynes. *J. Am. Chem. Soc.* **2017**, *139*, 7294−7301.

(11) Molnár, Á.; Sárkány, A.; Varga, M. Hydrogenation of Carbon−Carbon Multiple Bonds: Chemo-, Regio- and Stereo-Selectivity. *J. Mol. Catal. A: Chem.* **2001**, *173*, 185−221.

(12) Borodziński, A.; Bond, G. C. Selective Hydrogenation of Ethyne in Ethene-Rich Streams on Palladium Catalysts. Part 1. Effect of Changes to the Catalyst During Reaction. *Catal. Rev.* **2006**, *48*, 91−144.

(13) Borodziński, A.; Bond, G. C. Selective Hydrogenation of Ethyne in Ethene-Rich Streams on Palladium Catalysts, Part 2: Steady-State Kinetics and Effects of Palladium Particle Size, Carbon Monoxide, and Promoters. *Catal. Rev.* **2008**, *50*, 379−469.

(14) Boitiaux, J. P.; Cosyns, J.; Vasudevan, S. Hydrogenation of Highly Unsaturated Hydrocarbons over Highly Dispersed Palladium Catalyst: Part I: Behaviour of Small Metal Particles. *Appl. Catal.* **1983**, *6*, 41−51.

(15) Boitiaux, J. P.; Cosyns, J.; Vasudevan, S. Hydrogenation of Highly Unsaturated Hydrocarbons over Highly Dispersed Pd Catalyst.: Part II: Ligand Effect of Piperidine. *Appl. Catal.* **1985**, *15*, 317−326.

(16) Bos, A. N. R.; Westerterp, K. R. Mechanism and Kinetics of the Selective Hydrogenation of Ethyne and Ethene. *Chem. Eng. Process. Process. Intensif.* **1993**, *32*, 1−7.

(17) Molero, H.; Bartlett, B. F.; Tysoe, W. T. The Hydrogenation of Acetylene Catalyzed by Palladium: Hydrogen Pressure Dependence. *J. Catal.* **1999**, *181*, 49−56.

(18) Borodziński, A.; Cybulski, A. The Kinetic Model of Hydrogenation of Acetylene−Ethylene Mixtures over Palladium Surface Covered by Carbonaceous Deposits. *Appl. Catal., A* **2000**, *198*, 51−66.

(19) Zea, H.; Lester, K.; Datye, A. K.; Rightor, E.; Gulotty, R.; Waterman, W.; Smith, M. The Influence of Pd−Ag Catalyst Restructuring on the Activation Energy for Ethylene Hydrogenation in Ethylene−Acetylene Mixtures. *Appl. Catal., A* **2005**, *282*, 237−245.

(20) García-Mota, M.; Bridier, B.; Pérez-Ramírez, J.; López, N. Interplay between Carbon Monoxide, Hydrides, and Carbides in Selective Alkyne Hydrogenation on Palladium. *J. Catal.* **2010**, *273*, 92−102.

(21) McCue, A. J.; Anderson, J. A. Recent Advances in Selective Acetylene Hydrogenation Using Palladium Containing Catalysts. *Front. Chem. Sci. Eng.* **2015**, *9*, 142−153.

(22) Maeland, A. J.; Gibb, T. R. P. X-Ray Diffraction Observations of the Pd-H2 System Through the Critical Region. *J. Phys. Chem. A.* **1961**, *65*, 1270−1280.
(23) Jewell, L. L.; Davis, B. H. Review of Absorption and Adsorption in the Hydrogen−Palladium System. *Appl. Catal., A* **2006**, *310*, 1−15.
(24) Worsham, J. E.; Wilkinson, M. K.; Shull, C. G. Neutron-Diffraction Observations on the Palladium-Hydrogen and Palladium-Deuterium Systems. *J. Phys. Chem. Solids* **1957**, *3*, 303−310.
(25) Nelin, G. A Neutron Diffraction Study of Palladium Hydride. *Phys. Status Solidi B* **1971**, *45*, 527−536.
(26) Doyle, A. M.; Shaikhutdinov, S. K.; Freund, H. J. Alkene Chemistry on the Palladium Surface: Nanoparticles vs Single Crystals. *J. Catal.* **2004**, *223*, 444−453.
(27) Teschner, D.; Vass, E.; Hävecker, M.; Zafeiratos, S.; Schnörch, P.; Sauer, H.; Knop-Gericke, A.; Schlögl, R.; Chamam, M.; Wootsch, A.; Canning, A. S.; Gamman, J. J.; Jackson, S. D.; McGregor, J.; Gladden, L. F. Alkyne Hydrogenation over Pd Catalysts: A New Paradigm. *J. Catal.* **2006**, *242*, 26−37.
(28) Armbrüster, M.; Behrens, M.; Cinquini, F.; Föttinger, K.; Grin, Y.; Haghofer, A.; Klötzer, B.; Knop-Gericke, A.; Lorenz, H.; Ota, A.; Penner, S.; Prinz, J.; Rameshan, C.; Révay, Z.; Rosenthal, D.; Rupprechter, G.; Sautet, P.; Schlögl, R.; Shao, L.; Szentmiklósi, L.; Teschner, D.; Torres, D.; Wagner, R.; Widmer, R.; Wowsnick, G. How to Control the Selectivity of Palladium-based Catalysts in Hydrogenation Reactions: The Role of Subsurface Chemistry. *ChemCatChem* **2012**, *4*, 1048−1063.
(29) Neurock, M.; van Santen, R. A. A First Principles Analysis of C−H Bond Formation in Ethylene Hydrogenation. *J. Phys. Chem. B* **2000**, *104*, 11127−11145.
(30) Hansen, E. W.; Neurock, M. First-Principles-Based Monte Carlo Simulation of Ethylene Hydrogenation Kinetics on Pd. *J. Catal.* **2000**, *196*, 241−252.
(31) Neurock, M. Perspectives on the First Principles Elucidation and the Design of Active Sites. *J. Catal.* **2003**, *216*, 73−88.
(32) Sheth, P. A.; Neurock, M.; Smith, C. M. A First-Principles Analysis of Acetylene Hydrogenation over Pd(111). *J. Phys. Chem. B* **2003**, *107*, 2009−2017.
(33) Mei, D.; Sheth, P. A.; Neurock, M.; Smith, C. M. First-Principles-Based Kinetic Monte Carlo Simulation of the Selective Hydrogenation of Acetylene over Pd(111). *J. Catal.* **2006**, *242*, 1−15.
(34) Moskaleva, L. V.; Chen, Z.-X.; Aleksandrov, H. A.; Mohammed, A. B.; Sun, Q.; Rösch, N. Ethylene Conversion to Ethylidyne over Pd(111): Revisiting the Mechanism with First-Principles Calculations. *J. Phys. Chem. C* **2009**, *113*, 2512−2520.
(35) Yang, B.; Burch, R.; Hardacre, C.; Headdock, G.; Hu, P. Influence of Surface Structures, Subsurface Carbon and Hydrogen, and Surface Alloying on the Activity and Selectivity of Acetylene Hydrogenation on Pd Surfaces: A Density Functional Theory Study. *J. Catal.* **2013**, *305*, 264−276.
(36) Huang, S.-D.; Shang, C.; Kang, P.-L.; Zhang, X.-J.; Liu, Z.-P. LASP: Fast global potential energy surface exploration. *WIREs Comput. Mol. Sci.* **2019**, *9*, No. e1415.
(37) Ma, S.; Huang, S.-D.; Liu, Z.-P. Dynamic coordination of cations and catalytic selectivity on zinc−chromium oxide alloys during syngas conversion. *Nat. Catal.* **2019**, *2*, 671−677.
(38) Kang, P.-L.; Shang, C.; Liu, Z.-P. Glucose to 5-Hydroxymethylfurfural: Origin of Site-Selectivity Resolved by Machine Learning Based Reaction Sampling. *J. Am. Chem. Soc.* **2019**, *141*, 20525−20536.
(39) Shang, C.; Liu, Z.-P. Stochastic Surface Walking Method for Structure Prediction and Pathway Searching. *J. Chem. Theory Comput.* **2013**, *9*, 1838−1845.
(40) Zhang, X.-J.; Shang, C.; Liu, Z.-P. From Atoms to Fullerene: Stochastic Surface Walking Solution for Automated Structure Prediction of Complex Material. *J. Chem. Theory Comput.* **2013**, *9*, 3252−3260.
(41) Shang, C.; Zhang, X.-J.; Liu, Z.-P. Stochastic Surface Walking Method for Crystal Structure and Phase Transition Pathway Prediction. *Phys. Chem. Chem. Phys.* **2014**, *16*, 17845−17856.
(42) Huang, S.-D.; Shang, C.; Zhang, X.-J.; Liu, Z.-P. Material Discovery by Combining Stochastic Surface Walking Global Optimization with a Neural Network. *Chem. Sci.* **2017**, *8*, 6327−6337.
(43) Huang, S.-D.; Shang, C.; Kang, P.-L.; Liu, Z.-P. Atomic Structure of Boron Resolved Using Machine Learning and Global Sampling. *Chem. Sci.* **2018**, *9*, 8644−8655.
(44) Shang, C.; Huang, S.-D.; Liu, Z.-P. Massively Parallelization Strategy for Material Simulation Using High-Dimensional Neural Network Potential. *J. Comput. Chem.* **2019**, *40*, 1091−1096.
(45) Ma, S.; Shang, C.; Liu, Z.-P. Heterogeneous catalysis from structure to activity via SSW-NN method. *J. Chem. Phys.* **2019**, *151*, No. 050901.
(46) Zhang, X.-J.; Shang, C.; Liu, Z.-P. Double-Ended Surface Walking Method for Pathway Building and Transition State Location of Complex Reactions. *J. Chem. Theory Comput.* **2013**, *9*, 5745−5753.
(47) Zhang, X.-J.; Liu, Z.-P. Variable-Cell Double-Ended Surface Walking Method for Fast Transition State Location of Solid Phase Transitions. *J. Chem. Theory Comput.* **2015**, *11*, 4885−4894.
(48) Shang, C.; Liu, Z.-P. Constrained Broyden Minimization Combined with the Dimer Method for Locating Transition State of Complex Reactions. *J. Chem. Theory Comput.* **2010**, *6*, 1136−1144.
(49) Shang, C.; Liu, Z.-P. Constrained Broyden Dimer Method with Bias Potential for Exploring Potential Energy Surface of Multistep Reaction Process. *J. Chem. Theory Comput.* **2012**, *8*, 2215−2222.
(50) Kresse, G.; Joubert, D. From Ultrasoft Pseudopotentials to the Projector Augmented-Wave Method. *Phys. Rev. B* **1999**, *59*, 1758−1775.
(51) Kresse, G.; Furthmüller, J. Efficient Iterative Schemes for Ab Initio Total-Energy Calculations Using a Plane-Wave Basis Set. *Phys. Rev. B* **1996**, *54*, 11169−11186.
(52) Perdew, J. P.; Burke, K.; Ernzerhof, M. Generalized Gradient Approximation Made Simple. *Phys. Rev. Lett.* **1996**, *77*, 3865−3868.
(53) Lide, R. D. *CRC Handbook of Chemistry and Physics*, 84th ed.; CRC Press: New York, 2003−2004.
(54) Tang, Q.-L.; Hong, Q.-J.; Liu, Z.-P. CO2 Fixation into Methanol at Cu/ZrO2 Interface from First Principles Kinetic Monte Carlo. *J. Catal.* **2009**, *263*, 114−122.
(55) Caputo, R.; Alavi, A. L. I. Where do the H Atoms Reside in PdHx Systems? *Mol. Phys.* **2003**, *101*, 1781−1787.
(56) Grönbeck, H.; Zhdanov, V. P. Effect of Lattice Strain on Hydrogen Diffusion in Pd: A Density Functional Theory Study. *Phys. Rev. B* **2011**, *84*, No. 052301.
(57) Houari, A.; Matar, S. F.; Eyert, V. Electronic Structure and Crystal Phase Stability of Palladium Hydrides. *J. Appl. Phys.* **2014**, *116*, No. 173706.
(58) Niu, Y.; Liu, X.; Wang, Y.; Zhou, S.; Lv, Z.; Zhang, L.; Shi, W.; Li, Y.; Zhang, W.; Su, D. S.; Zhang, B. Visualizing Formation of Intermetallic PdZn in a Palladium/Zinc Oxide Catalyst: Interfacial Fertilization by PdHx. *Angew. Chem.* **2019**, *131*, 4276−4281.
(59) Yang, J.; Lv, C.-Q.; Guo, Y.; Wang, G.-C. A DFT+U Study of Acetylene Selective Hydrogenation on Oxygen Defective Anatase (101) and Rutile (110) TiO2 Supported Pd4 Cluster. *J. Chem. Phys.* **2012**, *136*, No. 104107.
(60) Horiuti, I.; Polanyi, M. Exchange Reactions of Hydrogen on Metallic Catalysts. *Trans. Faraday Soc.* **1934**, *30*, 1164−1172.
(61) Zhang, Q.; Li, J.; Liu, X.; Zhu, Q. Synergetic Effect of Pd and Ag Dispersed on Al2O3 in the Selective Hydrogenation of Acetylene. *Appl. Catal., A* **2000**, *197*, 221−228.
(62) Kuo, C.-T.; Lu, Y.; Kovarik, L.; Engelhard, M.; Karim, A. M. Structure Sensitivity of Acetylene Semi-Hydrogenation on Pt Single Atoms and Subnanometer Clusters. *ACS Catal.* **2019**, *9*, 11030−11041.
(63) Ma, H.-Y.; Wang, G.-C. Selective Hydrogenation of Acetylene on Ptn/TiO2 (n = 1, 2, 4, 8) Surfaces: Structure Sensitivity Analysis. *ACS Catal.* **2020**, *10*, 4922−4928.
(64) Li, Y.-F.; Liu, Z.-P. Particle Size, Shape and Activity for Photocatalysis on Titania Anatase Nanoparticles in Aqueous Surroundings. *J. Am. Chem. Soc.* **2011**, *133*, 15743−15752.
(65) Wei, G.-F.; Liu, Z.-P. Restructuring and Hydrogen Evolution on Pt Nanoparticle. *Chem. Sci.* **2015**, *6*, 1485−1490.

https://dx.doi.org/10.1021/acscatal.0c02158
ACS Catal. 2020, 10, 9694−9705

(66) Bunting, R. J.; Cheng, X.; Thompson, J.; Hu, P. Amorphous Surface PdOX and Its Activity toward Methane Combustion. *ACS Catal.* **2019**, *9*, 10317−10323.
(67) Cheng, X.; Wang, Z.; Mao, Y.; Hu, P. Evidence of the O−Pd−O and Pd−O4 Structure Units as Oxide Seeds and Their Origin on Pd(211): Revealing the Mechanism of Surface Oxide Formation. *Phys. Chem. Chem. Phys.* **2019**, *21*, 6499−6505.
(68) Hammer, B.; Nørskov, J. K. Theoretical Surface Science and Catalysis-Calculations and Concepts. *Advances in Catalysis*; Academic Press, 2000; Vol. *45*, pp 71−129.
(69) Huang, D. C.; Chang, K. H.; Pong, W. F.; Tseng, P. K.; Hung, K. J.; Huang, W. F. Effect of Ag-Promotion on Pd Catalysts by XANES. *Catal. Lett.* **1998**, *53*, 155−159.
(70) Shaikhutdinov, S.; Heemeier, M.; Bäumer, M.; Lear, T.; Lennon, D.; Oldman, R. J.; Jackson, S. D.; Freund, H. J. Structure−Reactivity Relationships on Supported Metal Model Catalysts: Adsorption and Reaction of Ethene and Hydrogen on Pd/Al2O3/NiAl(110). *J. Catal.* **2001**, *200*, 330−339.

https://dx.doi.org/10.1021/acscatal.0c02158
ACS Catal. 2020, 10, 9694−9705